# The 2023 Southeast Türkiye Seismic Sequence: Rupture of a Complex Fault Network

Gesa Maria Petersen[*1] , Pinar Büyükakpinar[1,2] , Felipe Orlando Vera Sanhueza[1,3] , Malte Metz[1,2] , Simone Cesca[1] , Kenan Akbayram[4,5] , Joachim Saul[1] , and Torsten Dahm[1,2]

## Abstract

On 6 February 2023, southeastern Türkiye experienced two $M_w$ 7.7 and 7.6 earthquakes. The earthquake sequence caused widespread damage and tens of thousands of casualties in Türkiye and Syria. We analyze mainshocks and aftershocks, combining complementary source characterization techniques, relying on local, regional, and teleseismic data. Backprojection analysis and finite source inversion for the mainshocks resolve coseismic slip, rupture length, and propagation mode along the main faults, whereas centroid moment tensor inversion for 221 aftershocks resolves details of the fault network. The first mainshock nucleated on a splay fault and activated the neighboring East Anatolian fault zone (EAFZ). It ruptured bilaterally along ∼500 km first toward northeast and later to south-southwest on multiple, previously partly dormant fault segments. The second mainshock ruptured the east–west-oriented Sürgü-Misis fault zone (SMFZ), reaching a slip of 7 m. The analysis of aftershocks with heterogeneous moment tensors retrospectively reconstructs rupture details. Along the main strand of the EAFZ, they map the geometry of different segments in unprecedented detail, whereas along the SMFZ they illuminate the geometry and behavior of large structures for the first time. Our work sheds light on multiple aspects of rupture evolution and provides new insights into the devastating earthquake sequence.

## Introduction

Southeastern Türkiye recently hosted two devastating earthquakes—$M_w$ 7.7 and 7.6—on 6 February 2023 (Fig. 1). The first earthquake (01:17:35 UTC; GEOFON) nucleated ∼20 km off the main strand of the East Anatolian fault zone (EAFZ) along a northeast–southwest-oriented splay fault (Melgar et al., 2023; Okuwaki et al., 2023), after an 8–10 months period of elevated seismicity (Kwiatek et al., 2023; Picozzi and Iaccarino, 2023). The splay fault rupture propagated to the main strand of the EAFZ (hereafter main EAFZ) rupturing the Amanos, Pazarcik, and Erkenek segments (Fig. 1) in a complex, multiphase, segmented rupturing process (Okuwaki et al., 2023; Zahradník et al., 2023). The second mainshock occurred 9 hr later (10:24:50 UTC; GEOFON) ∼100 km north of the first epicenter, close to an east–west-striking northern strand of the EAFZ, known as the Sürgü-Misis fault zone (SMFZ).

The EAFZ and the North Anatolian fault zone (NAFZ, inset in Fig. 1) are the major transform faults that accommodate the convergence of the Arabian and Eurasian plates leading to the westward motion of the Anatolian block (e.g., McClusky, et al., 2000; Şengör et al., 2005). The EAFZ (Fig. 1) is a segmented
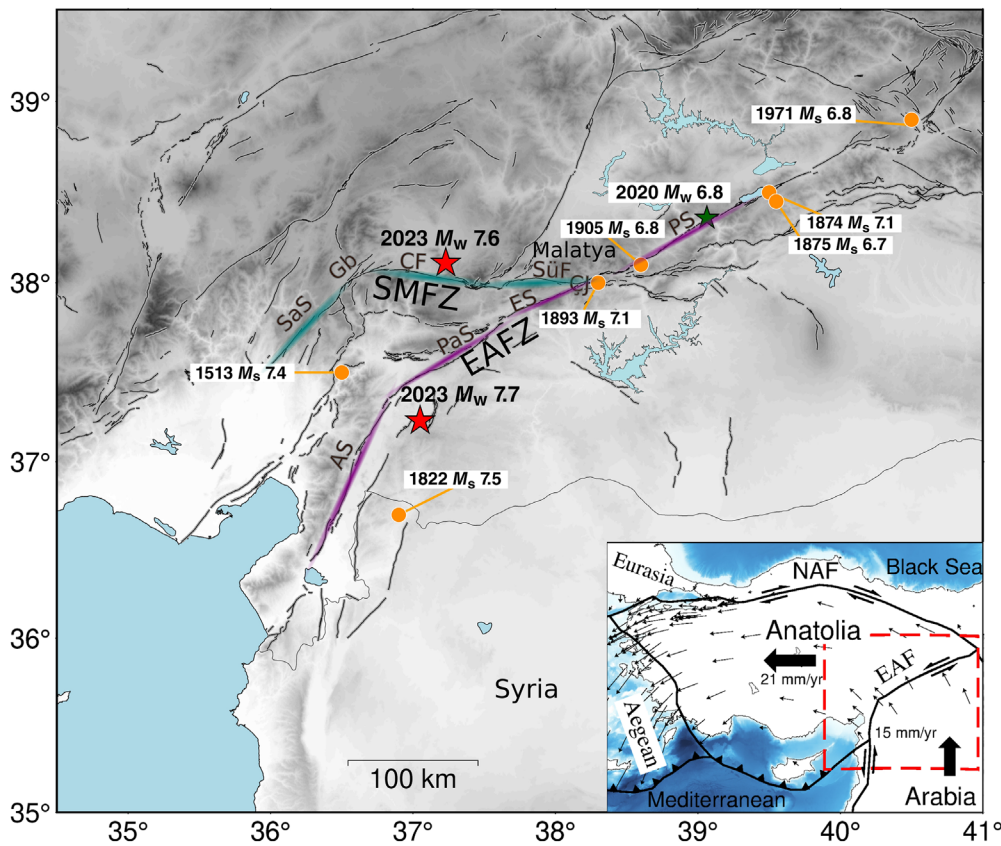
**Figure 1.** Map of the study region showing fault systems (Duman and Emre, 2013) and major earthquakes (orange circles; Ambraseys, 1989) along the East Anatolian fault zone (EAFZ). The first 2023 earthquake ruptured the main segments of the EAFZ (magenta), the second the Sürgü-Misis fault zone (SMFZ; cyan). Red stars show mainshock epicenters. The 2020 $M_w$ 6.8 Elazığ-Sivrice earthquake (green star) occurred northeast of the 2023 mainshocks. EAFZ fault segments: AS, Amanos; Cj, Çelikhan junction; ES, Erkenek; PaS, Pazarcik; PS, Pütürge. SMFZ segments: CF, Çardak fault; Gb, Göksun bend; SaS, Savrun segment; and SüF, Sürgü fault (Duman and Emre, 2013). The inset illustrates the main tectonic elements and their relative movement. Plate convergence rates from McClusky et al. (2000).

rate of 2.5 mm/yr was reported along the Çardak fault (Duman and Emre, 2013), on which an $M_s$ 5.8 earthquake occurred in 1986 (Taymaz et al., 1991).

In the last decade, the EAFZ showed a relatively low seismicity, with 11 earthquakes above $M_w$ 5 (catalog of the Turkish Disaster and Emergency Management Authority [AFAD]). In 2020, the $M_w$ 6.8 Elazığ-Sivrice earthquake ruptured the Pütürge segment ~230 km northeast of the first 6 February 2023 mainshock epicenter (e.g., Pousse-Beltran et al., 2020). Focal mechanisms of 2007–2020 earthquakes with $M_w \geq 3.5$ (Güvercin et al., 2022) show a majority of strike-slip mechanisms in the northeast segments of the main EAFZ and more normal faulting toward southwest. Little is known on focal mechanisms along the SMFZ, with only few solutions reported (Güvercin et al., 2022) and low seismicity rates.

This study aims to reconstruct co- and postseismic rupture processes of the 2023 earthquakes in southeast Türkiye. The mainshock analysis using backprojection and finite-fault inversion resolves the extent, geometry, and temporal evolution of the coseismic motion, whereas centroid moment tensor (CMT) inversions of aftershocks until 28 February 2023 help map the geometry of the activated fault network.

## Methods
### Mainshocks: Backprojection and finite-fault inversion

Backprojection exploits the coherence of short-period waveforms at teleseismic arrays (e.g., Ishii et al., 2005; Krüger and Ohrnberger, 2005) to image the earthquake rupture. We use a multiarray backprojection (Vera et al., 2022),

left-lateral strike-slip fault zone of ~580 km length (Duman and Emre, 2013), which experienced seven damaging ($M_s \geq 6.7$) earthquakes between 1513 and 1971 (Fig. 1; Ambraseys, 1989). The Global Positioning System slip rates across the main EAFZ change from ~10 mm/yr in the north-eastern part to ~4.5 mm/yr in southern segments (Aktug et al., 2016). Aktug et al. (2016) reported two seismic gaps on the main EAFZ with earthquake potential of $M_w$ 7.4 and 7.7.

The SMFZ (Fig. 1) is a segmented ~350 km long fault system west of the EAFZ (Duman and Emre, 2013). Its eastern strand extends east–west over ~140 km, terminating to the east at the Çelikhan junction with the EAFZ. The main segments are the Sürgü and Çardak faults (Fig. 1), which are separated by a bend with complex faults (Duman and Emre, 2013). A slip

stacking weighted backprojections in moving time windows from arrays under different azimuths (6 s window length, time-steps of 1 s, 20% threshold of radiated energy; Figs. S1–S4, available in the supplemental material to this article). The rupture is tracked by locating semblance maxima, whereas the short-period source time function is the beam power energy as a function of time. We backprojected $P$ waves (0.75–2.0 Hz) from vertical velocity seismograms recorded by three arrays (Hi-net, Alaska, and the USArray; see Data and Resources). Theoretical $P$-wave arrival times were corrected using an aftershock-based calibration method and GEOFON epicenters (Palo *et al.*, 2014; Table S1). We use a secondary grid when energy emissions originate from more than one main direction at the same time (see rectangle in Fig. S1a).

Finite-fault inversions can cross validate backprojection results (Metz *et al.*, 2022), quantify the major slip segment, slip amplitude, location, orientation and geometry of the rupture, and provide first-order estimates of the rupture velocity. We resolve these parameters performing single-plane quasi-dynamic probabilistic finite-fault inversions (Heimann *et al.*, 2018; Dahm *et al.*, 2021; Metz *et al.*, 2022), combining vertical and transverse full waveforms from 20 teleseismic broadband stations (0.003–0.01 Hz), and vertical and radial components of 15 near-field strong-motion records (0.01–0.05 Hz; see Data and Resources; Figs. S5–S8). The low-frequency range stabilizes static parameters but results in a limited resolution of dynamic parameters such as origin and rupture velocity. Each fault is defined by $6 \times 4$ slip patches with uniform stress drop, balancing resolution and computation time. Waveforms are modeled by discretizing the subfault plane into multiple equally spaced CMTs. Vertical and horizontal spacings between these sources are governed by the spacing of the Green's function grid size (1 km).

### Moment tensor inversion of fore- and aftershocks

We invert CMTs for 222 earthquakes with $M_w \geq 3.7$ using the probabilistic inversion tool Grond (Heimann *et al.*, 2018). We fit three-component full waveform displacements and amplitude spectra of broadband regional data, with epicentral distances below 500 km (Fig. S9; see Data and Resources). Clipped, incomplete, and noisy waveforms were manually removed. Average source parameters and uncertainties are estimated by bootstrapping, and only stable results with consistent mean and best solutions are reported. Synthetic seismograms are computed using QSEIS (Wang, 1999) and CRUST2.0 regional velocity models (Bassin *et al.*,

2000). Separate inversions are performed for pure double couple (DC), deviatoric, and full moment tensor (MT) sources.

## Results

All backprojection, finite-fault inversion, and CMT results are provided in the supplemental material and in a complementary data publication (see Data and Resources).

### Mainshocks

Backprojection and finite-fault inversion reveal a complex bilateral rupture for the first mainshock (Fig. 2, Movie S1). The earthquake ruptured ~560 km length during 117 s. We identify four phases based on observations of rupture direction and the energy radiated source time function (Fig. 2). In phase I, the rupture propagates unilaterally ~130 km toward northeast over ~40 s. In phase II, ~50 s after the nucleation, the rupture continues bilaterally toward northeast and southwest (Movie S1) but predominantly toward southwest. Toward northeast, the rupture extended ~270 km from the epicenter, partially overlapping with the rupture of the 2020 $M_w$ 6.8 Elazığ-Sivrice earthquake (Fig. S1). This extent is not a "swimming" artifact in the direction of the array, because it is also seen when excluding the Hi-net array that is located close to the strike direction of the EAFZ (Fig. S10). In phase III, at 65–90 s the rupture continued unilaterally toward southwest, focusing near the coastline at ~36° E. In the last rupture phase IV (108–117 s), the short-period emissions reached off the coast of Latakia, Syria. The last phase is visible as a secondary maximum after a stopping phase for >10 s.

The maximum rupture speed from high-frequency emissions during the first mainshock is 3.4 km/s (Fig. S1c), similar to the crustal shear wave velocity from the CRUST2.0 (3.5 km/s) velocity model. The average rupture speed (1.8 km/s) is significantly lower.

The finite-fault inversion resolves a rupture plane striking northeast (57 ± 3°) and dipping 82 ± 5° (Fig. S11, Table S2). Average rupture speed, maximum slip and magnitude are 2.6 ± 0.4 km/s, 4.0 ± 2.6 m, and $M_w$ 7.8, respectively. The inferred fault plane corresponds to the region of the highest short-period energy emission from the backprojection. Uncertainties of the centroid location result from using long-periodic, teleseismic surface-wave data. Compared to the GEOFON mechanism, a rotation of ~30° results from using different inversion approaches and input datasets with GEOFON using $P$ waves.

For the second earthquake ($M_w$ 7.6, 10.24 UTC), the backprojection resolved an east–west bilateral rupture with a preferred eastward propagation over ~115 km within 32 s (Fig. 2, Fig. S3, Movie S2). First the emissions are focused up to ~30 km west of the epicenter (0–17 s) and later propagated eastward (18–32 s). We resolve a fast, but subshear (~95% $V_S$), maximum rupture speed of 3.2 km/s (average speed 2.1 km/s). The finite-fault inversion for the second earthquake identifies an east–west-oriented fault plane (strike 92 ± 2°) dipping 73 ± 6° with a length of 93 ± 18 km and a width of 17 ± 7 km. The rupture initiates in the shallow central part, and propagates bilaterally toward east and west, lasting overall 25 s, with 7.1 ± 2.6 m average slip. The finite-fault inversion confirms subshear velocity, with an average rupture speed of 2.1 km/s.
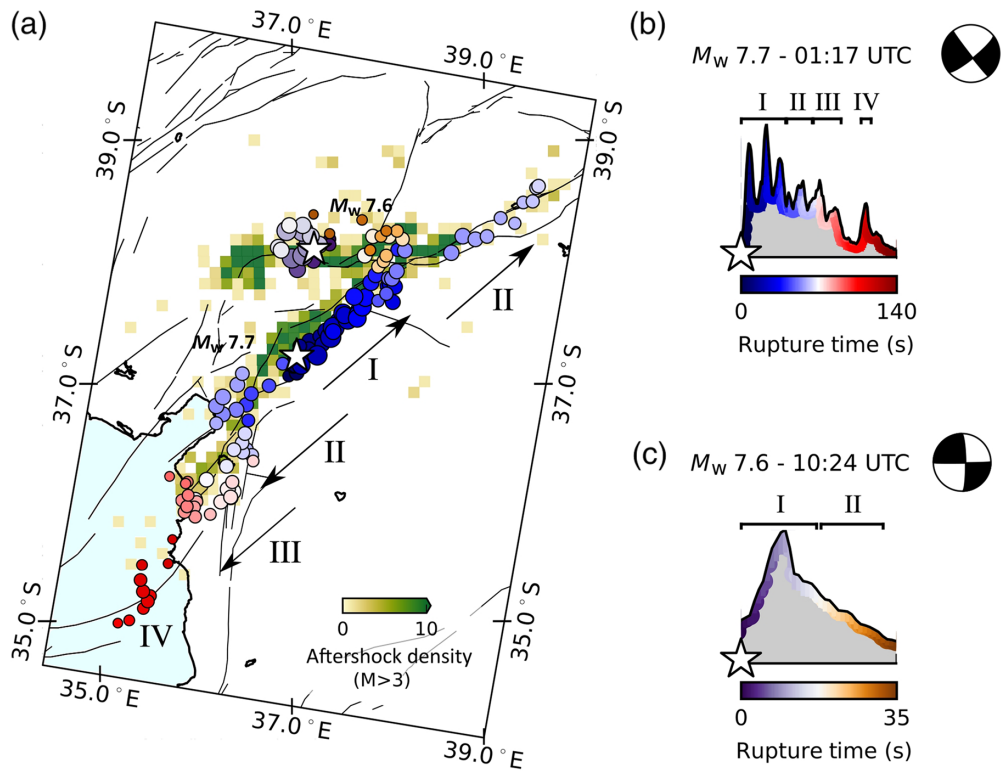


**Figure 2.** Backprojection results for the $M_w$ 7.7 and 7.6 earthquakes on 6 February 2023 in southeastern Türkiye; frequency band 0.75–2 Hz. (a) Map showing backprojected energy emissions (circles), colored relative to the mainshock origin times and scaled to relative energy release. The rupture origins of both the events are shown as stars. The yellow to green background colors indicate the density of aftershocks (M ≥ 3) during the first week from the disaster and emergency management authority (AFAD) catalog. The arrows with roman numbers indicate major rupture propagation phases of the first mainshock. (b,c) Normalized energy release over time for both the events shown as shaded areas. Moment tensors (MTs) and origins from GEOFON, fault database from Styron and Pagani (2020).

## CMT inversion of aftershocks

Full MT solutions for one foreshock and 221 aftershocks until 28 February 2023 show a high variability in mechanisms. Strike-slip faulting with northeast–southwest-oriented pressure axes is dominant along the Sürgü and Çardak faults (Fig. 3, profile B0–B1) and on a northeast oriented, previously unmapped fault close to Malatya (B1–B2). Despite being separated by only ~25 km, the parallel fault segments of the northeastern EAFZ (central part of A1–A2) shows variable mechanisms with strike-slip, normal, and a few thrust events. Principal axes are consistent along both the fault segments, with northeast–southwest pressure and northwest–southeast tension axes. Normal faulting is observed especially west of ~37° E, both on the southwest branch of the EAFZ (A0–A1) and at the westernmost N45°E to north–south-oriented part of the SMFZ. In contrast, the northeastern part of the

main EAFZ (Fig. 3, A1–A2) hosts multiple thrust faulting events, together with left-lateral strike slips.

Pure DC, deviatoric, and full MT solutions (see also Data and Resources) are coherent in terms of DC orientations. Full MTs indicate minor but robust isotropic components, whereas compensated linear vector dipoles are poorly resolved (Fig. S12). The spatial distribution of isotropic components shows positive isotropic components for normal to oblique faulting at the western end of the SMFZ and in the southwest part of the EAFZ (Fig. S12a), indicating small opening processes. Negative isotropic components are found for thrust to oblique earthquakes along the northeast part of the EAFZ (Fig. S12b). Although our observations illustrate consistent features with faulting type, a more detailed uncertainty analysis on the non-DC is required in future work.
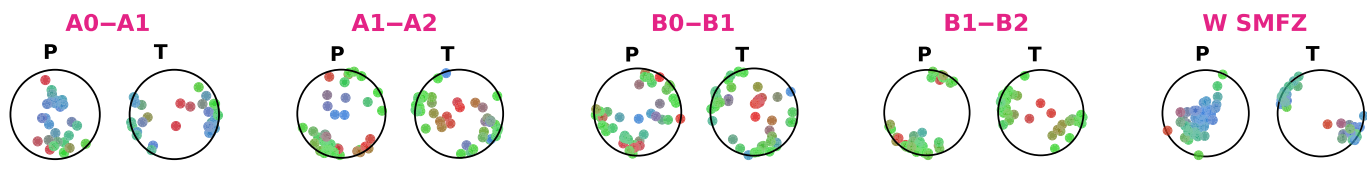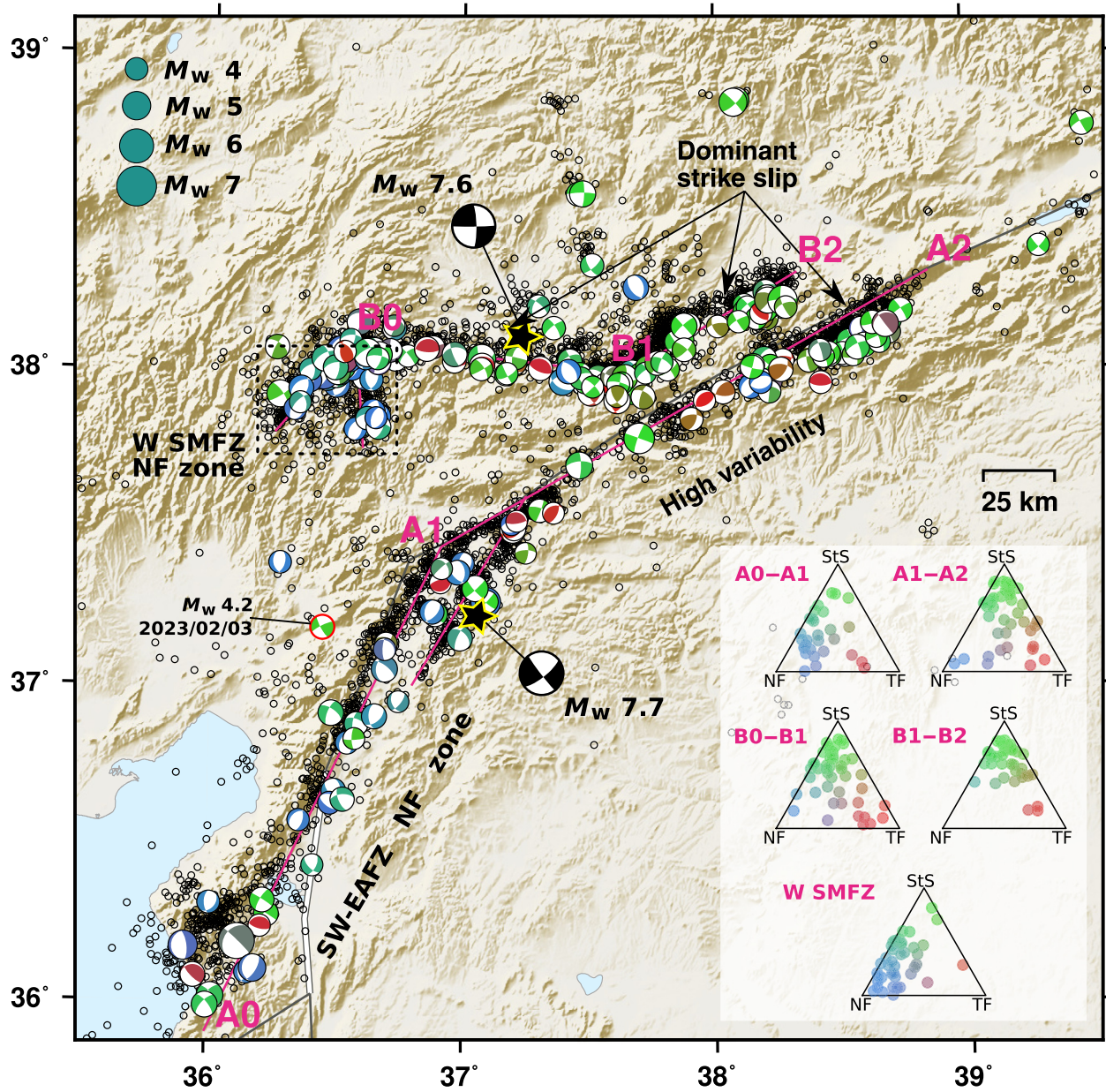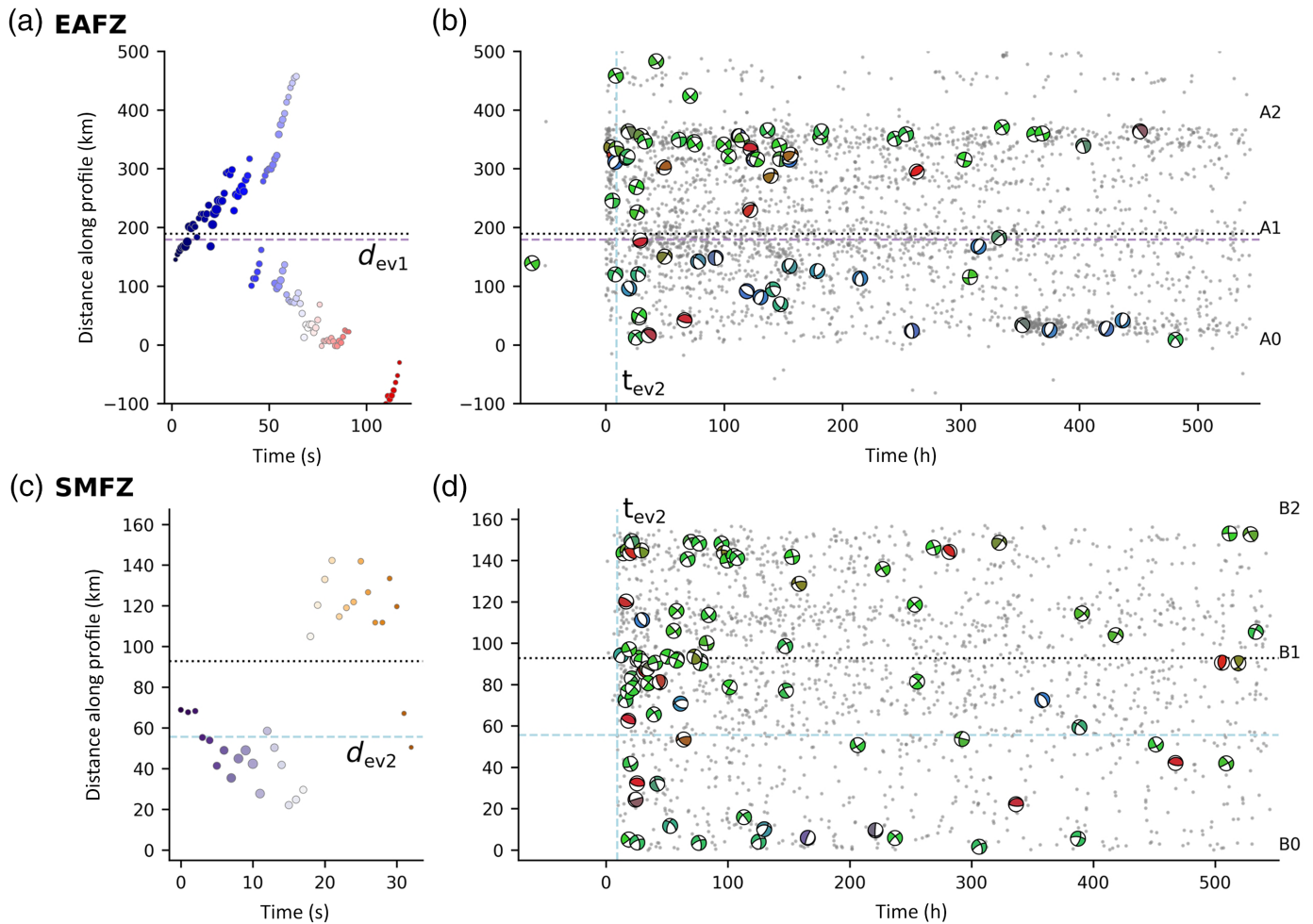
**Figure 3.** Double-couple MTs for one foreshock and 221 aftershocks of the 2023 Türkiye earthquakes ($M_w$ ≥ 3.7). Colors indicate rupturing mechanisms (pure strike slips [StS] in green, normal faulting [NF] in blue and thrust faulting [TF] in red). The hypocenters of the two mainshocks (stars) shown for comparison, MTs from GEOFON. Annotations refer to features described in CMT Inversion of aftershocks and the Discussion. The inset shows mechanism type diagrams for the defined profiles (A, B) and the western (W) SMFZ. Pressure (P) and tension (T) axis are shown below the map. Note that the different faulting regimes on the fault segments are still observed for aftershocks with $M_w$ ≥ 4.5.

**Figure 4.** Rupture process and aftershock time series. (a,c) Short-period backprojected rupture of the first and second mainshock over time, projected along profiles A0–A1–A2 and B0–B1–B2, respectively. Profile A0–A1–A2 was extended to northeast and southwest to cover the full extent of the backprojected energy. Colors indicate time for comparison with same color scales as in Figure 2b,c. (b,d) MTs of this study projected to the same profiles. Time is relative to the origin time of the first mainshock. The blue vertical lines show the timing of the second mainshock ($t_{ev2}$), the purple, and blue horizontal lines show the locations of the first ($d_{ev1}$) and second mainshock ($d_{ev2}$) on profile A and B, respectively. The black horizontal lines indicate where strike direction of profiles change (point A1, B1 in Fig. 3).

## Discussion

The 2023 seismic sequence exceeded the magnitude of any known prior earthquake in the region, including the 1822 $M_s \sim 7.5$ Aafrine earthquake (Fig. 1; Ambraseys, 1989). The occurrence of two large earthquakes within a short-time interval (~9 hr) is infrequent but not rare (Kagan and Jackson, 1999). The repeated strong ground shaking attributed to the two mainshocks likely strongly impacted building and infrastructure damages (e.g., Mignan *et al.*, 2018).

The joined spatiotemporal analysis of backprojected energy and aftershock focal mechanisms shed light on the rupturing process (Fig. 4). The bilateral rupture of the first event from backprojection extended over >450 km during ~90 s. Subsequently, after >10 s quiescence, the rupture continued offshore adding ~100 km. In comparison, the aftershocks are mainly distributed over ~360 km (profile A0–A1–A2, Fig. 4b), whereas a surface rupture of ~300 km was measured in the field (K. Akbayram, personal comm., 2023). At the

northeast and southwest edges of the backprojected rupture aftershock seismicity is very low.

Despite the small magnitude difference ($M_w$ 7.7 and 7.6), the second mainshock activated a significantly shorter fault plane than the first. Backprojection results (Fig. 4c) and aftershock locations (Fig. 4d) cover a fault length of ~160 km along two segments with different orientations (Fig. 3). The event did

not rupture the westernmost part of the SMFZ, where a significant normal-faulting aftershock activity is observed (Figs. 2, 3). Based on scaling relations (Blaser et al., 2010), the expected strike-slip rupture length for magnitude $M_w$ 7.7 and $M_w$ 7.6 earthquakes are 163 km and 142 km, respectively. For the first mainshock this value significantly underestimates the activated fault length from backprojection, aftershocks, and field observations. We attribute the discrepancy to spatial heterogeneity of coupled fault segments. The heterogeneous energy emission source time function (Fig. 2b) supports the idea of a subsequent rupturing of heterogeneous segments.

The two mainshocks ruptured two differently oriented faults. The temporal evolution of the rupture processes jumping over different structures with different faulting styles is similar, for example, to the 2002 Denali, Alaska, or the 2016 Kaikōura, New Zealand, earthquakes, for which a large variability of aftershock mechanisms was also observed (Cesca et al., 2017; Eberhart-Phillipps et al., 2003). Similar to the mainshock nucleation, the single $M_w > 4$ foreshock on 3 February 2023 did not rupture the EAFZ. Instead, it was located ~30 km west of it.

The heterogeneity of aftershock mechanisms, involving strike-slip, normal and thrust faulting, is an interesting characteristic of the 2023 sequence that points toward the activation of numerous fault segments and variable stress regimes along the long fault systems. We observe temporal and spatial variability in the moment release of different fault patches (Fig. S13) as well as a difference in predominant focal mechanisms (Figs. 3, 4). Within six hours after the first mainshock, the high aftershock rate with many overlapping events reduced the completeness of our MT catalog. The aftershock activity of the first mainshock was limited to the EAFZ: before the $M_w$ 7.6 event on the SMFZ no $M_w > 3.5$ event occurred in that region. Strike-slip aftershocks, similar to the focal mechanisms of the respective mainshocks, were predominant on both the fault systems during the first two days. Although strike slip remained as the dominant rupture type on the central SMFZ (Fig. 4b), normal faulting became more common on the southwest branch of the EAFZ after three days (A0–A1 in Fig. 4a). Thrust faulting is observed especially during the first days on profile B0–B1–B2 and is less frequent afterward (Fig. 4d).

Although the aftershocks in the vicinity of the fault segments of the first mainshock show a larger variability of focal mechanisms, those of the second mainshock are more similar, showing predominantly strike-slip mechanisms. An exception are clusters of normal-faulting earthquakes at the western termination of the SMFZ, which are in agreement with the

westernmost subevent inversion result of the $M_w$ 7.6 earthquake by Zahradník et al. (2023).

The previous earthquake source studies already revealed the heterogeneity of focal mechanisms in the EAFZ (e.g., Güvercin et al., 2022), which has been attributed to geometrical complexities in the segmentation of the EAFZ, changes in the stress field, and a weak coupling among different fault segments (Güvercin et al., 2022). MTs for the time period 2007–2020 (Güvercin et al., 2022) show predominant strike-slip faulting along the north-eastern branch of EAFZ and dominant normal faulting to the southwest (Fig. S14). This pattern is similar to our inversion results for the 2023 sequence, for which MTs reveal a transition from a transtensional (normal to strike-slip mechanisms) to transpressional (strike slip to thrust mechanisms) tectonic domain along the EAFZ at ~37° E longitude. Notably, the MT catalog by Güvercin et al. (2022) includes only a few mechanisms along the SMFZ. Based on a few mechanisms they concluded a left-lateral movement, whereas a right-lateral movement was also discussed in the earlier studies (e.g., Koç and Kaymakcı, 2013). The 129 MT solutions along the SMFZ (B0–B1–B2) of this study image the slip geometry of the SMFZ in unprecedented detail and confirm the left-lateral movement, which is also observed in the second mainshock.

Both the local variability of dominant DC faulting of the aftershocks and their non-DC components can be explained in the context of the fault geometry and the regional tectonic setting. The northward movement of the Arabian plate relative to the Anatolian block results in the observed left-lateral strike-slip mechanism of the first mainshock and parts of the aftershocks on the EAFZ. The change in strike direction along the main EAFZ—from ~north–south at its southern end to northeast–southwest at its northern termination against the NAFZ—is accompanied by compression, explaining the occurrence of thrust faulting and negative isotropic components in the northeast of the study area. In contrast, the escape movement of the Anatolian block toward the west results in normal-faulting mechanisms and positive isotropic components in the south-western part of the study area. Irregular occurrences of normal faulting earthquakes along the northeast part of the main EAFZ may suggest pull-apart movements along the strike-slip fault, which, over long time periods, for example, formed Lake Hazar (Duman and Emre, 2013). Although strike-slip faulting along the east–west branch of the SMFZ is in agreement with the previous studies, seismicity and slip rates have been particularly low in the last decades (e.g., Duman and Emre, 2013; Güvercin et al., 2022). The aftershock sequence of the second mainshock provides

for the first time detailed insights into the rupturing of the SMFZ and a previously unmapped, northeast-oriented fault segment close to Malatya (profile B1–B2 in Fig. 3). Normal faulting in the westernmost activated part of the SMFZ results from the eastward movement of the southern block causing extensional stress on the northeast–southwest-striking faults.

Finally, although the investigation of the triggering process of the first and the second mainshock remains beyond the scope of the study, we point out that both the events did not initiate on the main EAFZ, which is interesting and has implications for hazard estimates and early warning systems. We are convinced that our results can facilitate future detailed studies on the interaction of fault segments and triggering processes.

## Conclusions

On 6 February 2023, two major earthquakes with $M_w$ 7.7 and 7.6 led to devastating destruction, and tens of thousands of casualties in Türkiye and Syria. We used multiple source inversion techniques to investigate the rupture process of mainshocks and aftershocks, and the active fault systems. We study the evolution of the seismic sequence over different time scales, with the main ruptures lasting seconds to minutes and the aftershocks study period covering the first three weeks. The first mainshock ruptured multiple segments of the main branch of the EAFZ, which accommodates the northward motion of the Arabic plate relative to Anatolia with a left-lateral strike-slip fault system. The second mainshock activated the SMFZ, the northern strand off the EAFZ with an east–west strike direction in its central part. The backprojection analysis reveals the bilateral rupture propagation of both the mainshocks across multiple fault segments and provides insights into the spatiotemporal rupture evolution.

The backprojection showed a complex rupture for the first event, affecting over 500 km from the 2020 Elazığ-Sivrice earthquake in the northeast to the region off the coast of Latakia, Syria in the southwest. The second event ruptured a significantly shorter, east–west-oriented fault (∼160 km). Full MT solutions of 222 fore- and aftershocks complement the seismological analysis, revealing the geometry and motion of different faults and fault segments. Strike-slip faulting is mostly observed in the central and eastern parts of the SMFZ, and in the first days along the EAFZ. The westernmost active part of the SMFZ and later events in the southwestern EAFZ have predominant normal-faulting mechanisms with positive isotropic components, which we attribute to extensional processes accompanying the westward movement of Anatolia. In contrast, compression in the northeast EAFZ leads to thrust faulting and negative isotropic components. The large number of aftershock mechanisms provide detailed insights into active fault segments, some of which had not shown significant seismic activity for decades. The catalog of MT solutions and the results of the backprojection analysis (see Data and Resources) will support subsequent studies of stress transfer among faults and fault segments, and facilitate new hazard estimates.

## Data and Resources

The moment tensor (MT) inversion and backprojection results are open to the public as a data publication at doi: 10.5281/zenodo.7861735 (Petersen *et al.*, 2023). MT inversion files contain results for double couple (DC), deviatoric, and full inversions; backprojection results include energy release time series with locations, the source time functions of radiated energy, and the semblance maxima for the 2023 Türkiye $M_w$ 7.7 and 7.6 earthquakes. All seismic data used for MT and finite-fault inversion (Table 1) is openly available from GEOFON data center (https://geofon.gfz-potsdam.de/), Incorporated Research Institutions for Seismology (IRIS; https://ds.iris.edu/ds/nodes/dmc/data/types/waveform-data/), Turkish Disaster and Emergency Management Authority (AFAD; https://tdvms.afad.gov.tr/continuous_data), and Kandilli Observatory and Earthquake Research Institute (KOERI; https://www.koeri.boun.edu.tr). We thank the National Research Institute for Earth Science and Disaster Prevention (NIED) for making Hi-net data available, retrieved using the HinetPy Python package (Tian, 2020). Topographic data (Figs. 1, 3): SRTM (Farr *et al.*, 2007), faults and plate boundaries: Bird (2003), Styron and Pagani (2020). The seismic catalog is openly available from AFAD (https://deprem.afad.gov.tr/event-catalog). The supplemental material includes additional figures, movies and tables that provide more detailed insights into the analyzed data sets and results and that support the discussion in the main paper. All websites were last accessed in March 2023.

## Declaration of Competing Interests

The authors acknowledge that there are no conflicts of interest recorded.

## Acknowledgments

## Table 1
**Overview of Seismic Datasets Used in This Study**

| Method | Network Code | Data Type | DOI or Reference Link |
|---|---|---|---|
| Backprojection | Hi-net | SA | https://www.hinet.bosai.go.jp, doi: 10.1186/BF03353076, doi: 10.1063/1.1854197 |
| | Alaska (AK, AT, AV) | SA | AK: doi: 10.7914/SN/AK, AT: doi: 10.7914/SN/AT, AV: doi: 10.7914/SN/AV |
| | USArray (CN, IM, NM, and US) | SA | CN: doi: 10.7914/SN/CN, IM: http://service.iris.edu/fdsnws/dataselect/1/ (last accessed March 2023) and https://www.fdsn.org/networks/detail/IM/ (last accessed May 2023), NM: https://www.memphis.edu/ceri/seismic/index.php (last accessed April 2023), US: doi: 10.7914/SN/US |
| Finite-fault inversion | AF | BB | doi: 10.7914/SN/AF |
| | DK | BB | GEUS Geological Survey of Denmark and Greenland (1976). Danish Seismological Network |
| | EI | BB | doi: 10.7914/SN/EI |
| | HE | BB | doi: 10.14470/UR044600 |
| | II | BB | doi: 10.7914/SN/II |
| | IU | BB | doi: 10.7914/SN/IU |
| | KO | BB | doi: 10.7914/SN/KO |
| | KC | BB | doi: 10.7914/SN/KC |
| | PM | BB | doi: 10.7914/SN/PM |
| | WM | BB | doi: 10.14470/JZ581150 |
| | TK | ACC | doi: 10.7914/SN/TK |
| Moment tensor inversion | KO | BB | doi: 10.7914/SN/KO |
| | TU | BB | doi: 10.7914/SN/TU |
| | GE | BB | doi: 10.14470/TR560404 |
| | IU | BB | doi: 10.7914/SN/IU |

ACC, accelerometric stations; BB, broadband stations; and SA, seismic array.

## References

Aktug, B. A., H. Ozener, A. Dogru, A. Sabuncu, B. Turgut, K. Halicioglu, O. Yilmaz, and E. Havazli (2016). Slip rates and seismic potential on the East Anatolian Fault System using an improved GPS velocity field, J. Geodynam. 94, 1–2.

Ambraseys, N. N. (1989). Temporary seismic quiescence: SE Turkey, Geophys. J. Int. 96, 311–331, doi: 10.1111/j.1365-246X.1989.tb04453.x.

Bassin, C., G. Laske, and G. Masters (2000). The current limits of resolution for surface wave tomography in North America, Eos Trans. AGU 81, F897, doi: 10.4236/ijmnta.2016.51003.

Bird, P. (2003). An updated digital model of plate boundaries, Geochem. Geophys. Geosys. 4, 1027, doi: 10.1029/2001GC000252.

Blaser, L., F. Krüger, M. Ohrnberger, and F. Scherbaum (2010). Scaling relations of earthquake source parameter estimates with special focus on subduction environment, Bull. Seismol. Soc. Am. 100, no. 6, 2914–2926.

Cesca, S., Y. Zhang, V. Mouslopoulou, R. Wang, J. Saul, M. Savage, S. Heimann, S.-K. Kufner, O. Oncken, and T. Dahm (2017). Complex rupture process of the Mw 7.8, 2016, Kaikoura earthquake, New Zealand, and its aftershock sequence, *Earth Planet. Sci. Lett.* **478,** 110–120.

Dahm, T., S. Heimann, M. Metz, and M. P. Isken (2021). A self-similar dynamic rupture model based on the simplified wave-rupture analogy, *Geophys. J. Int.* **225,** 1586–1604, doi: 10.1093/gji/ggab045.

Duman, T. Y., and Ö. Emre (2013). The East Anatolian fault: Geometry, segmentation and jog characteristics, *Geol. Soc. Lond. Spec. Publ.* **372,** 495–529.

Eberhart-Phillips, D., P. J. Haeussler, J. T. Freymueller, A. D. Frankel, C. M. Rubin, P. Craw, N. A. Ratchkovski, G. Anderson, G. A. Carver, A. J. Crone, *et al.* (2003). The 2002 Denali Fault earthquake, Alaska: A large magnitude, slip-partitioned event, *Science* **300,** no. 5622, 1113–1118, doi: 10.1126/science.1082703.

Farr, T. G., P. A. Rosen, E. Caro, R. Crippen, R. Duren, S. Hensley, M. Kobrick, M. Paller, E. Rodriguez, L. Roth, *et al.* (2007). The shuttle radar topography mission, *Rev. Geophys.* **45,** RG2004 , doi: 10.1029/2005RG000183.

Güvercin, S. E., H. Karabulut, A. O. Konca, U. Doğan, and S. Ergintav (2022). Active seismotectonics of the East Anatolian Fault, *Geophys. J. Int.* **230,** no. 1, 50–69, doi: 10.1093/gji/ggac045.

Heimann, S., M. Isken, D. Kühn, H. Sudhaus, A. Steinberg, S. Daout, S. Cesca, H. Vasyura-Bathke, and T. Dahm (2018). Grond - A probabilistic earthquake source inversion framework V. 1.0, *GFZ Data Service*, doi: 10.5880/GFZ.2.1.2018.003.

Ishii, M., P. M. Shearer, H. Houston, and J. E. Vidale (2005). Extent, duration and speed of the 2004 Sumatra–Andaman earthquake imaged by the Hi-Net array, *Nature* **435,** no. 7044, 933–936.

Kagan, Y. Y., and D. D. Jackson (1999). Worldwide doublets of large shallow earthquakes, *Bull. Seismol. Soc. Am.* **89,** no. 5, 1147–1155, doi: 10.1785/BSSA0890051147.

Koç, A., and N. Kaymakcı (2013). Kinematics of Sürgü fault zone (Malatya, Turkey): A remote sensing study, *J. Geodynam.* **65,** 292–307, doi: 10.1016/j.jog.2012.08.001.

Krüger, F., and M. Ohrnberger (2005). Tracking the rupture of the Mw= 9.3 Sumatra earthquake over 1,150 km at teleseismic distance, *Nature* **35,** no. 7044, 937–939.

Kwiatek, G., P. Martínez-Garzón, D. Becker, G. Dresen, F. Cotton, G. C. Beroza, D. Acarel, S. Erginatav, and M. Bohnhoff (2023). Months-long preparation of the 2023 Mw 7.8 Kahramanmaras earthquake, Türkiye, preprint, submitted to Nature, doi: 10.21203/rs.3.rs-2657873/v1.

Mcclusky, S., S. Balassanian, A. Barka, C. Demir, S. Ergintav, I. Georgiev, O. Gurkan, M. Hamburger, K. Hurst, H. Kahle, *et al.* (2000). Global positioning system constraints on plate kinematics and dynamics in the Eastern Mediterranean and Caucasus, *J. Geophys. Res.* **105,** 5695–5719, doi: 10.1029/1999JB900351.

Melgar, D., T. Taymaz, A. Ganas, B. Crowell, T. Öcalan, M. Kahraman, V. Tsironi, S. Yolsal-Çevikbilen, S. Valkaniotis, T. S. Irmak, *et al.* (2023). Sub- and super-shear ruptures during the 2023 Mw 7.8 and Mw 7.6 earthquake doublet in SE Türkiye, *Seismica* **2,** no. 3, doi: 10.26443/seismica.v2i3.387.

Metz, M., F. Vera, A. Carrillo Ponce, S. Cesca, A. Babeyko, T. Dahm, J. Saul, and F. Tilmann (2022). Seismic and tsunamigenic characteristics of a multimodal rupture of rapid and slow stages: The example of the complex 12 August 2021 South Sandwich earthquake, *J. Geophys. Res.* **127,** e2022JB024646, doi: 10.1029/2022JB024646.

Mignan, A., L. Danciu, and D. Giardini (2018). Considering large earthquake clustering in seismic risk analysis, *Nat. Hazards* **91,** no. 2018, 149–172, doi: 10.1007/s11069-016-2549-9.

Okuwaki, R., Y. Yagi, T. Taymaz, and S. P. Hicks (2023). Multi-scale rupture growth with alternating directions in a complex fault network during the 2023 south-eastern Türkiye and Syria earthquake doublet, preprint, doi: 10.31223/X5RD4W.

Palo, M., F. Tilmann, F. Krüger, L. Ehlert, and D. Lange (2014). High-frequency seismic radiation from Maule earthquake (Mw 8.8, 2010 February 27) inferred from high-resolution backprojection analysis, *Geophys. J. Int.* **199,** no. 2, 1058–1077.

Petersen, G., P. Büyükakpinar, F. Vera, M. Metz, S. Cesca, K. Akbayram, J. Saul, and T. Dahm (2023). Dataset of backprojection and MT inversion results for 2023 Türkiye earthquake sequence (Version 1) [Data set], *Zenodo*, doi: 10.5281/zenodo.7861735.

Picozzi, M., and A. Iaccarino (2023). The preparatory process of the 2023 Mw 7.8 Turkey earthquake, preprint, doi: 10.21203/rs.3.rs-2619572/v1.

Pousse-Beltran, L., E. Nissen, E. A. Bergman, M. D. Cambaz, É. Gaudreau, E. Karasözen, and F. Tan (2020). The 2020 M w 6.8 Elazığ (Turkey) earthquake reveals rupture behavior of the East Anatolian Fault, *Geophys. Res. Lett.* **47,** no. 13, e2020GL088136, doi: 10.1029/2020GL088136.

Şengör, A. M. C., O. Tüysüz, C. İmren, M. Sakınç, H. Eyidoğan, N. Görür, X. Le Pichon, and C. Rangin (2005). The north Anatolian fault: A new look, *Annu. Rev. Earth Planet. Sci.* **33,** no. 1, 37–112, doi: 10.1146/annurev.earth.32.101802.120415.

Styron, R., and M. Pagani (2020). The GEM global active faults database, *Earthq. Spectra* **36,** 160–180, doi: 10.1177/8755293020944182.

Taymaz, T., H. Eyidoğan, and J. Jackson (1991). Source parameters of large earthquakes in the East Anatolian Fault Zone (Turkey), *Geophys. J. Int.* **106,** no. 3, 537–550.

Tian, D. (2020). seisman/HinetPy: 0.6.6 (0.6.6), *Zenodo* doi: 10.5281/zenodo.3695076.

Vera, F., F. Tilmann, and J. Saul (2022). A decade of short-period earthquake rupture histories from multi-array back-projection, Authorea Preprints, available at https://d197for5662m48.cloudfront.net/documents/publicationstatus/112162/preprint_pdf/f95be4f05e69d902a8eb656893bb0773.pdf (last accessed April 2023).

Wang, R. (1999). A simple orthonormalization method for stable and efficient computation of Green's functions, *Bull. Seismol. Soc. Am.* **89,** no. 3, 733–741, doi: 10.1785/BSSA0890030733.

Zahradník, J., F. Turhan, E. Sokos, and F. Gallovič (2023). Asperity-like (segmented) structure of the 6 February 2023 Turkish earthquakes, preprint, doi: 10.31223/X5T666.